Abnormal vascularization in mouse retina with dysregulated retinal cholesterol homeostasis

Saida Omarova,[1] Casey D. Charvet,[1] Rachel E. Reem,[1] Natalia Mast,[1] Wenchao Zheng,[1] Suber Huang,[1,2] Neal S. Peachey,[3,4,5] and Irina A. Pikuleva[1]

[1]Department of Ophthalmology and Visual Sciences, Case Western Reserve University, Cleveland, Ohio, USA. [2]University Hospitals, Cleveland, Ohio, USA. [3]Cole Eye Institute, Cleveland Clinic Foundation, Cleveland, Ohio, USA. [4]Cleveland VA Medical Center, Cleveland, Ohio, USA. [5]Department of Ophthalmology, Cleveland Clinic Lerner College of Medicine, Case Western Reserve University, Cleveland, Ohio, USA.

Several lines of evidence suggest a link between age-related macular degeneration and retinal cholesterol maintenance. Cytochrome P450 27A1 (CYP27A1) is a ubiquitously expressed mitochondrial sterol 27-hydroxylase that plays an important role in the metabolism of cholesterol and cholesterol-related compounds. We conducted a comprehensive ophthalmic evaluation of mice lacking *CYP27A1*. We found that the loss of CYP27A1 led to dysregulation of retinal cholesterol homeostasis, including unexpected upregulation of retinal cholesterol biosynthesis. *Cyp27a1*$^{-/-}$ mice developed retinal lesions characterized by cholesterol deposition beneath the retinal pigment epithelium. Further, *Cyp27a1*-null mice showed pathological neovascularization, which likely arose from both the retina and the choroid, that led to the formation of retinal-choroidal anastomosis. Blood flow alterations and blood vessel leakage were noted in the areas of pathology. The *Cyp27a1*$^{-/-}$ retina was hypoxic and had activated Müller cells. We suggest a mechanism whereby abolished sterol 27-hydroxylase activity leads to vascular changes and identify *Cyp27a1*$^{-/-}$ mice as a model for one of the variants of type 3 retinal neovascularization occurring in some patients with age-related macular degeneration.

Introduction

Our sense of sight depends on a normally functioning retina, the light-sensitive tissue lining the inner surface of the eye. Of particular importance is the central macula, which is responsible for visual acuity and color vision. When the macula begins to degenerate, the affected individual loses central vision and the ability to read fine print and recognize faces. Age-related macular degeneration (AMD) is a major cause of irreversible vision loss and blindness in the elderly of industrialized countries (1).

AMD is a progressive disease manifested at late stages in 2 forms, non-neovascular and neovascular. The latter involves retinal vascular networks (Supplemental Figure 1A; supplemental material available online with this article; doi:10.1172/JCI63816DS1) and is classified into types 1, 2, and 3 (2, 3) based on anatomical position of the neovascular process relative to the retinal pigment epithelium (RPE), a monolayer of cells serving as an interface between the retina and choroid (4). In types 1 and 2, new blood vessels originate from the choroid and proliferate below (type 1) and above the RPE (type 2; Supplemental Figure 1, B and C). Type 2 neovascularization (NV), also called classic choroidal NV, represents the typical clinical course of neovascular AMD. In contrast, in type 3 NV, the proliferative activity can also occur within the retina and coexist with choroidal NV (Supplemental Figure 1, D and F, and ref. 3). A distinct feature of this type of NV is formation of retinal-choroidal anastomosis (RCA) (Supplemental Figure 1E), which aberrantly connects intraretinal and choroidal vascular networks that normally supply blood to the inner and outer retina, respectively. Type 3 NV, also referred to as retinal angiomatous proliferation (RAP), is present in 10% to 15% of neovascular AMD cases (5) and is a form of exudative AMD described only in the past decade (3). This form of NV is unique in terms of demographics, risk factors, clinical manifestations, disease course, and response to treatment (3).

The exact etiology of AMD is currently not fully understood, but is believed to be multifactorial, involving aging and interactions between genetic and environmental factors (6, 7). Cholesterol is somehow involved, as cholesterol-rich and lipid-rich extracellular lesions (drusen and basal linear deposits) are the hallmark features of early- and intermediate-stage AMD (8–10). The accumulation of drusen and basal linear deposits is a part of the normal aging process, yet in individuals with AMD, these lesions are larger in size and number. Although cholesterol and extractable lipids, particularly cholesterol esters, account for more than 40% of druse volume (10–12), population-based studies have failed to establish a clear association between serum lipid profiles and AMD (13–17). In contrast, genetic studies have identified several cholesterol-related genes (*apoE*, *CETP*, *ABCA1*, and *LIPC*) as risk factors for AMD (18–22). This apparent inconsistency suggests that the link between cholesterol and AMD is complex and likely involves disturbances in cholesterol homeostasis in the retina, a yet-under-investigated area in vision research (23). An important approach to bridging this gap involves ocular evaluation of genetically manipulated animals. To date, such studies have focused on mouse models with deficiencies in lipoprotein-mediated cholesterol transport (24, 25), and less attention has been paid to the enzymatic pathways by which cholesterol is eliminated from tissues.

Cytochrome P450 27A1 (CYP27A1) is a ubiquitous enzyme that catalyzes the hydroxylation of cholesterol and other sterols at position C27 and thereby plays an important role in bile acid biosynthesis in the liver, cholesterol removal from many extrahepatic tissues, and activation of vitamin D_3 in the kidney (26). We established that CYP27A1 is the principal cholesterol hydroxylase in the retina, where it accounts for the majority of enzymatic cholesterol elimination (27, 28). In humans, CYP27A1 deficiency leads to cerebrotendinous

Authorship note: Saida Omarova and Casey D. Charvet contributed equally to this work.

Conflict of interest: The authors have declared that no conflict of interest exists.

Citation for this article: *J Clin Invest.* 2012;122(8):3012–3023. doi:10.1172/JCI63816.

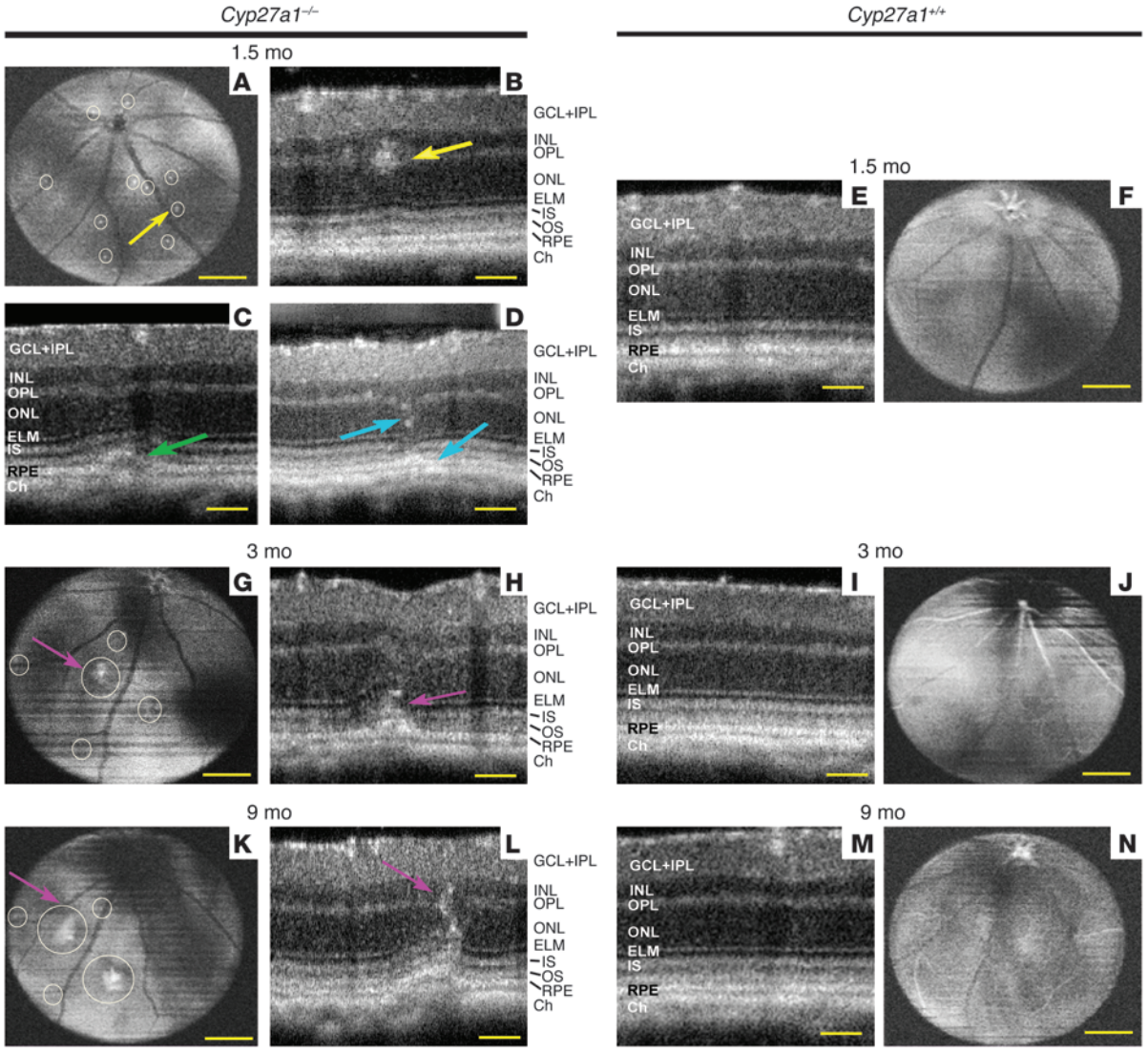

Figure 1

Age-dependent progression of retinal pathologies in *Cyp27a1*$^{-/-}$ mice. Representative OCT fundus depth images (50° field of view) at the OPL in *Cyp27a1*$^{-/-}$ (**A**, **G**, and **K**) and age- and sex-matched *Cyp27a1*$^{+/+}$ (**F**, **J**, and **N**) animals. Areas of pathology are circled, and those that were further examined by SD-OCT cross sections (**B**, **H**, and **L**) are marked with arrows; arrows of the same color indicate the same animal. Representative cross sections of the corresponding areas in *Cyp27a1*$^{+/+}$ animals (**E**, **I**, and **M**) are also shown. Labeling of retinal layers is based on hyper- and hyporeflective OCT bands. Scale bars: 300 μm (**A**, **F**, **G**, **J**, **K**, and **N**); 60 μm (**B**–**E**, **H**, **I**, **L**, and **M**).

xanthomatosis (CTX), a rare and multi-symptom lipid storage disease whose typical clinical features include juvenile bilateral cataracts, neurological dysfunction, and tendon xanthomas. CTX patients also complain of diarrhea and often have premature atherosclerosis and osteoporosis (29, 30). A number of ocular abnormalities have been reported, including cholesterol-like crystals in the vitreous, premature retinal senescence with drusen and retinal vessel sclerosis, cholesterol-like deposits along the vascular arcades, RPE defects on fluorescein angiography (FA), and optic disc pallor (31–33). These abnormalities indicate that CYP27A1 plays an important role in the retina and that a better understanding of the role of this enzyme will provide insight into the role of cholesterol in this organ.

Cyp27a1$^{-/-}$ mice have undergone extensive characterization (34–38). They lack classical symptoms of CTX, such as cataracts, brain and tendon xanthomas, and atherosclerosis, but reproduce several of the important biochemical changes observed in humans. Similar to humans, hepatic synthesis of cholesterol and bile acid intermediates is increased in *Cyp27a1*$^{-/-}$ mice, and the pool of bile acids is reduced. These animals also show accumulation of the cholesterol biohydrogenation product cholestanol in plasma and tissues when plasma levels of cholesterol are normal (34, 35, 37, 38). Changes in *Cyp27a1*$^{-/-}$ mice, however, are less pronounced than in humans and are thought to reflect distinct manifestations of sterol 27-hydroxylase deficiency in *Cyp27a1*$^{-/-}$ mice and CTX patients (36). Despite these differences, CTX patients and *Cyp27a1*$^{-/-}$ mice both exhibit dysregulated lipid metabolism. Here, we show that lack of Cyp27a1 in mice is associated with RCA as well as vascular leakage and focal depositions containing cholesterol along Bruch's membrane (BrM). We also provide a mechanistic explanation for the observed

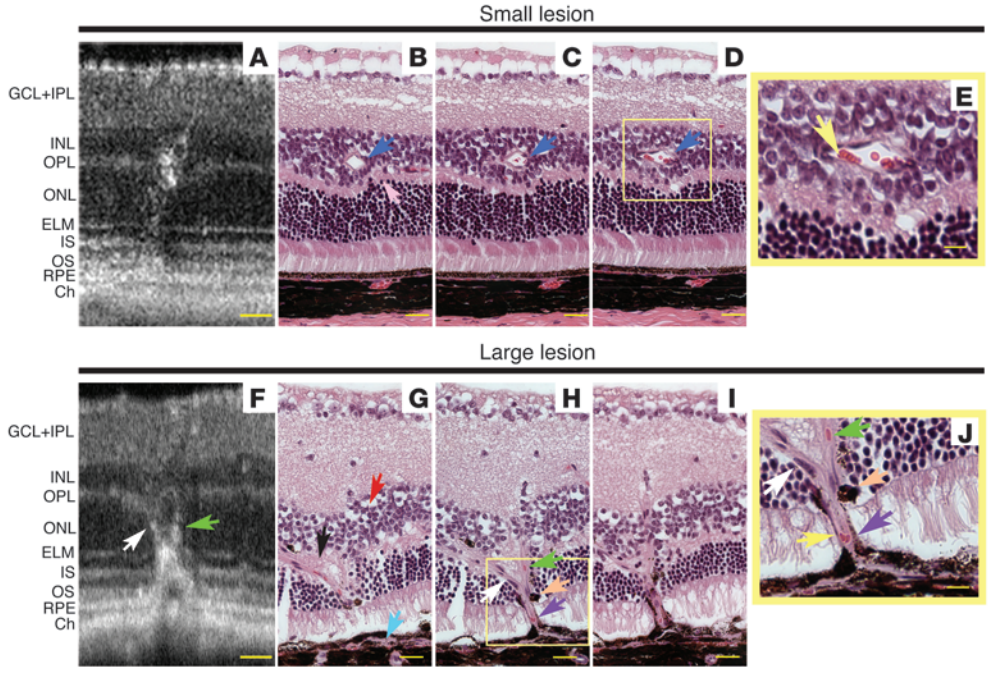

Figure 2
Distinct structures of small and large lesions in *Cyp27a1*$^{-/-}$ mice. (**A**) Representative SD-OCT cross section and (**B**–**E**) serial sections through a small hyperreflective spot. (**F**) SD-OCT cross section and (**G**–**J**) serial sections through a large hyperreflective spot. Dark blue arrows (**B**–**D**) indicate dilated structure in the INL; pink arrow (**B**) points to twisting of the OPL; yellow arrows (**E** and **J**) show red blood cells in blood vessels; white and green arrows (**F**, **H**, and **J**) mark the blood vessels growing into the ONL; black arrow (**G**) indicates fibrosis in the OPL; red arrow (**G**) points to a representative cystic space and edema of the INL; light blue arrow (**G**) indicates fibrovascular material above BrM; orange arrows (**H** and **J**) indicate RPE debris in the ONL; purple arrows (**H** and **J**) indicate merged blood vessel in the photoreceptor layer. Scale bars: 30 μm (**A**–**D**, **F**–**I**); 10 μm (**E** and **J**). Original magnification, ×400.

ocular phenotype. The data obtained advance our understanding of how disturbances in retinal cholesterol homeostasis may underlie neovascular forms of AMD, which are associated with the greatest risk of vision loss.

Results

In vivo imaging with ultra–high resolution spectral-domain optical coherence tomography. Spectral-domain optical coherence tomography (SD-OCT) fundus imaging of 1.5-month-old *Cyp27a1*$^{-/-}$ mice revealed small hyperreflective spots in the inferior retina (Figure 1A) that were not observed in the superior retina or in WT littermates (Figure 1F). In *Cyp27a1*$^{-/-}$ mice, the number of spots ranged from 3 to 10 per eye, with an average number of 5. When examined in cross section, most small spots had a major disturbance, hyperreflective whorl-like structure, in the outer plexiform layer (OPL) (Figure 1B) and a minor disturbance in the RPE. However, in some spots, the OPL was only slightly affected and the major abnormality was an elevation of the RPE (Figure 1C), a pattern similar to that of classic choroidal NV on SD-OCT (39). In some spots, hyperreflective disturbances occurred both in the RPE and in the outer layers of the neural retina (Figure 1D). The majority of spots did not change with age, although some grew in diameter, as observed in a representative *Cyp27a1*$^{-/-}$ mouse (Figure 1, G and K). Of the 5 circled lesions in this mouse, 2 subtended a larger retinal area and expanded within the retina to affect the inner retinal layers. (Figure 1, H and L). By 12 months, 63% of *Cyp27a1*$^{-/-}$ females (7/11) and 84% of *Cyp27a1*$^{-/-}$ males (16/19) had developed at least 1–2 large spots in both eyes.

Lesion structure. We investigated the structure of small and large spots by serial sectioning of paraffin-embedded eyes followed by H&E staining (Figure 2). Serial sectioning through a small lesion in an 8-month-old *Cyp27a1*$^{-/-}$ animal revealed OPL disruption and torsion near the inner nuclear layer/OPL (INL/OPL) interface (Figure 2B) and the presence of small eosin-positive round spheres in the INL (Figure 2E). We concluded that the small OPL lesions are abnormally dilated blood vessels (Figure 2, B–D), most of which do not change with age, as indicated by SD-OCT.

Histological examination of a large lesion in a representative 11-month-old *Cyp27a1*$^{-/-}$ mouse revealed formation of an RCA involving blood vessels between the INL and choroid (Figure 2, F–J). The origin of the RCA cannot be unequivocally determined. Therefore, we will describe this RCA as starting from the inner retina, although choroidal or simultaneous retinal and choroidal NV are also possible. The latter would be consistent with our OCT data showing simultaneous disturbances in the OPL and RPE in all studied young *Cyp27a1*$^{-/-}$ mice (Figure 1, B–D). In any case, in large lesions, we detected cystic spaces surrounding many nuclei within an edematous and vacuolated INL (Figure 2G). The OPL was disorganized and fibrotic, and thickened fibrovascular material was noted between the RPE and BrM (Figure 2G). This fibrovascular material seemed to displace the reactive RPE into the region normally occupied by the outer segment (OS) and inner segment (IS). Branches arising from the blood vessels in the INL likely grew through the fibrotic OPL, merged into a single vessel (Figure 2, H and J) at the outer nuclear layer/IS (ONL/IS) region, which is normally avascular, and then traversed the OS and RPE to form an RCA with the choriocapillaris. The presence of red blood cells (Figure 2J) in the lumen of this blood vessel supports our interpretation of this structure as a patent RCA. There are also signs of RPE cell migration adjacent to this vessel in the ONL (Figure 2H), which may be a result of higher (relative to the retina) choroidal blood flow displacing RPE cells into the OPL. This local RPE detachment is not an artifact of tissue processing and sectioning because similar detachments are detected by volume cross-section reconstruction generated by SD-OCT imaging of a live animal (Supplemental Video 1). In a different and older 14-month-old *Cyp27a1*$^{-/-}$ mouse, we noted similar but more severe structural abnormalities (Supplemental Figure 2), in which the INL edema was greater, vascularization extended to

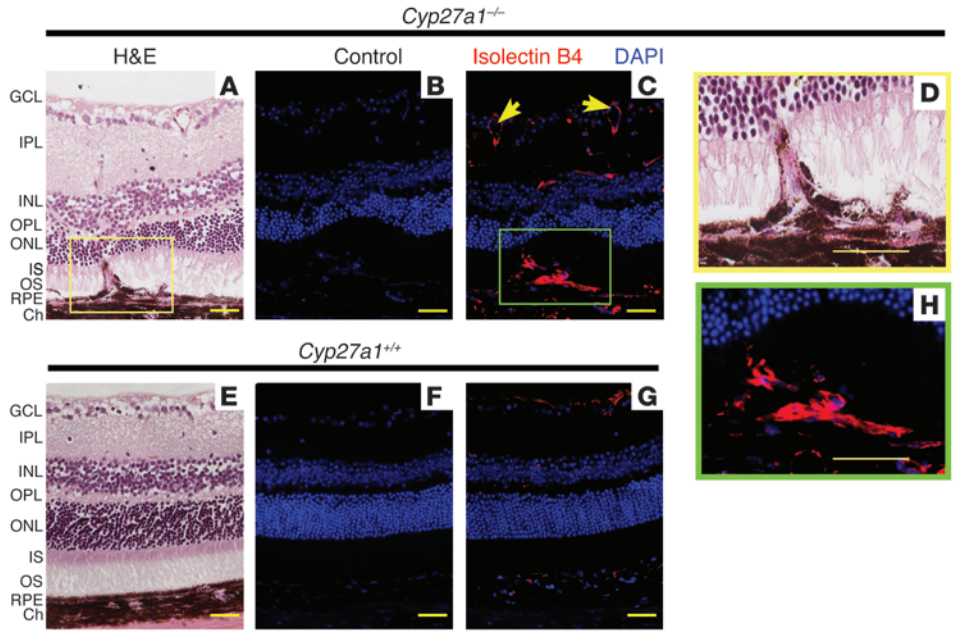

Figure 3
Focal choroidal NV in *Cyp27a1*$^{-/-}$ mice. Panels are representative of stainings carried out on adjacent sections cut through pathologies in *Cyp27a1*$^{-/-}$ mice (**A**–**D**, and **H**) or through a corresponding region in *Cyp27a1*$^{+/+}$ mice (**E**–**G**). (**A**, **D**, and **E**) H&E staining. (**C**, **G**, and **H**) Staining with isolectin B4, a marker for blood vessels, conjugated to DyLight 594 fluorophore (in red); nuclei were stained with DAPI (in blue). **D** and **H** are enlarged areas of **A** and **C**, respectively. **B** and **F** are control sections with isolectin B4 omitted. Yellow arrows (**C**) indicate blood vessels in the GCL. Scale bars: 30 μm. Original magnification, ×400.

the inner plexiform layer (IPL), fibrosis in the OPL and RPE was more pronounced, the RPE displacement was more substantial, and the RCA affected a greater area of the RPE.

SD-OCT imaging and H&E staining demonstrated that the retinal lesions occupy a small retinal area. Consistent with this, electroretinography (ERG) measurements were mostly similar in *Cyp27a1*$^{-/-}$ and WT mice (Supplemental Figure 3), indicating generally normal overall retinal function.

Retinal vasculature and Müller cells. Abnormal retinal vascularization was further confirmed by staining with isolectin B4, a marker of endothelial cells lining blood vessels (40). A fluorescent signal was observed where blood vessels are normally present — in the ganglion cell layer (GCL), IPL, INL, OPL, and choroid of *Cyp27a1*$^{-/-}$ and WT (Figure 3, C and G) mice. The overall intensity of the signal was much higher in the GCL of *Cyp27a1*$^{-/-}$ than in WT retina, probably reflecting blood vessel dilation (Figure 3C). Isolectin B4 also labeled the *Cyp27a1*$^{-/-}$ outer retina, which is normally avascular (Figure 3C). When compared against the adjacent H&E-stained section (Figure 3A) and examined at higher magnification (Figure 3, D and H), this labeling was seen to correspond to an RCA between the choroidal and retinal vasculature. Staining with a different blood vessel marker, tomato lectin, and of different *Cyp27a1*$^{-/-}$ mice also revealed abnormal retinal vascularization (Figure 4). In this example, the RCA spans the retina from the choroid to the retinal blood supply located in the GCL (Figure 4).

We examined Müller cells, the predominant glial cell type of the retina, as they are reported to play a role in NV (41, 42). We labeled Müller cells with glutamine synthase (GS) and glial fibrillary acidic protein (GFAP). GS is expressed constitutively in Müller cells (43), whereas GFAP is an intermediate filament protein upregulated in Müller cells in response to hypoxia, injury, and photoreceptor degeneration (44). Staining for GFAP was also reported in the RPE cells of patients with AMD (45). Anti-GFAP immunoreactivity was very low in the WT retina (Figure 4L), but was elevated in *Cyp27a1*$^{-/-}$ animals in lesion areas (Figure 4D) and elsewhere (Figure 4G), indicating general activation of Müller cells throughout the *Cyp27a1*$^{-/-}$ retina. In both regions, GFAP activation was seen in the GCL. In the lesion area, GFAP activation was also observed along the RCA (in the INL, OPL, ONL, and RPE cells). In addition to Müller cell activation throughout the retina in *Cyp27a1*$^{-/-}$ mice, Müller cell bodies were also disorganized and gliotic, as indicated by immunolabeling with anti-GS (Figure 4, E and H).

For in vivo assessments, we used FA, in which intraperitoneal injection of a live animal with sodium fluorescein is followed by acquisition of fundus images by scanning laser ophthalmoscope. Representative images from 2 *Cyp27a1*$^{-/-}$ animals are shown to illustrate the abnormalities noted on FA (Figure 5). Figure 5B is an image focused on the GCL and taken 1 minute after injection. A bright spot (Figure 5B) corresponding to a lesion on SD-OCT (Figure 5C) and having indistinct margins is apparent, suggestive of increased vascular permeability. In this mouse, fluorescein leakage was not detected in retinal layers below the OPL, indicating either that the RCA is not yet formed in this lesion or that there is no blood flow through this area due to reactive fibrosis. The pathology also seems to affect the neighboring blood vessel, causing its attenuation and beading (Figure 5B). Similar changes were never seen in WT animals (Figure 5A). In the second *Cyp27a1*$^{-/-}$ animal, a hyperfluorescent spot was observed when the instrument was focused on the INL or the RPE 5 minutes after injection (Figure 5, D and E). The location of this hyperfluorescent spot matched a lesion detected by SD-OCT (Figure 5F). The appearance of this late focal hyperfluorescence in the INL and RPE layers, with indistinct margins, suggests the formation of RCA in this lesion accompanied by increased vascular permeability (46). In the 2 animals, the location of the lesions varied relative to the inner retinal vasculature. In one case (Figure 5B), it was near the major blood vessel, whereas in the other (Figure 5, D and E), it was near a branch of a blood vessel. The relationship between the location of these lesions relative to blood vessels remains to be established.

We examined retinal circulation of *Cyp27a1*$^{-/-}$ mice using Doppler flow of SD-OCT, which color codes direction and velocity of blood flow (Figure 6E). In the healthy vasculature of WT reti-

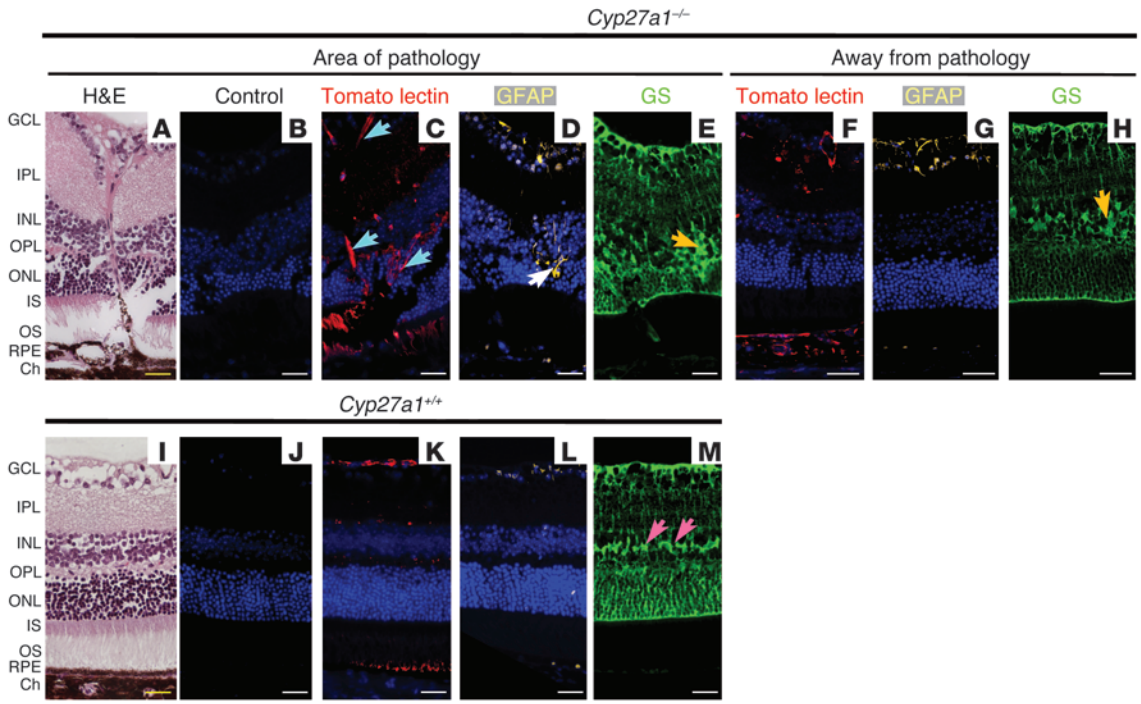

Figure 4

Focal intraretinal NV and Müller cell activation in *Cyp27a1*$^{-/-}$ mice. Panels are representative of stainings carried out on adjacent retinal sections in *Cyp27a1*$^{-/-}$ mice (**A**–**H**) or through corresponding regions in *Cyp27a1*$^{+/+}$ mice (**I**–**M**). (**A** and **I**) H&E staining. (**C**, **F**, and **K**) Stainings with a marker for blood vessels, tomato lectin (in red), which is a less specific blood-vessel marker than isolectin B4, binding to photoreceptors. (**D**, **G**, and **L**) Localization of GFAP, a marker of activated Müller cells (in yellow). (**E**, **H**, and **M**) Localization of GS expressed constitutively in Müller cells (in green). (**B** and **J**) Negative control sections treated with serum from nonimmunized animal. For fluorescent images, nuclei were stained with DAPI (in blue), and immunoreactivity/lectin binding was detected by DyLight 649–conjugated (in yellow), DyLight 549–conjugated (in red), and DyLight 488–conjugated (in green) fluorophores. Light blue arrows (**C**) indicate retinal blood vessels in different retinal layers; white arrow (**D**) indicates increased GFAP staining in the OPL and ONL in the area of pathology; gold arrows (**E** and **H**) indicate disorganized Müller cell bodies in *Cyp27a1*$^{-/-}$ specimen; and pink arrows (**M**) indicate proper organization of Müller cell bodies in *Cyp27a1*$^{+/+}$ specimen. Scale bars: 30 μm. Original magnification, ×400.

na, there was a mixed distribution of bright red and blue pixels, and the retinal and choroidal circulations were clearly separated (Figure 6D). In the *Cyp27a1*$^{-/-}$ animal, there was only 1 color, pale blue, in the lesion area (but not in the areas distal from the lesions), and the separation between the retinal and choroidal circulations broke down (Figure 6D) due to the presence of blood flow into the normally avascular ONL. Thus, Doppler flow of SD-OCT confirms that the RCAs observed in *Cyp27a1*$^{-/-}$ retinas by histology and FA are patent.

Hypoxia. Abnormal blood vessels may form secondary to impaired oxygenation or hypoxia (47). To investigate these, we used 2 different markers. Pimonidazole (Supplemental Figure 4) is an azole-containing small molecule and a sensor of absolute oxygen tensions. It is administered to live animals and binds to thiol-containing proteins in tissues with low, less than 14 mm Hg, oxygen tensions (48). In contrast, HIF-1A is a protein and transcription factor and a sensor of abnormal oxygen tensions (49, 50). The threshold oxygen tension for HIF-1A activation varies depending on cell type and is sometimes greater than 14 mmHg. If so, hypoxia is not detected by pimonidazole binding (50). Because of this and other differences, antipimonidazole and anti–HIF-1A stainings may not always colocalize (50–52). As compared with the WT retina (Figure 7E), antipimonidazole staining was increased in the IS and RPE in *Cyp27a1*$^{-/-}$ animals throughout the retina (Figure 7, C and D). Staining for HIF-1A was also increased throughout the *Cyp27a1*$^{-/-}$ retinas (Figure 7, H and I) and was particularly intense in the choroid near the RCA (Figure 7H). Thus, staining with pimonidazole and HIF-1A documents lowered oxygen tensions and generalized retinal hypoxia in the *Cyp27a1*$^{-/-}$ retina. While detectable, the level of hypoxia was not sufficient to impact overall retinal function, as ERGs of *Cyp27a1*$^{-/-}$ mice were generally normal (Supplemental Figure 3).

Lipid distribution. We used 2 lipid stains, oil red O, and filipin. Oil red O binds mainly to neutral lipids as well as fatty acids, whereas filipin interacts with sterols containing a free 3β-hydroxyl group including unesterified cholesterol (UC) (53). Esterified cholesterol can also be detected by filipin, but requires additional specimen extraction with ethanol and treatment with cholesterol esterase (54). In both *Cyp27a1*$^{-/-}$ and WT animals, faint oil red O staining was present in all retinal layers (Figure 8, B, D, H, and J). In *Cyp27a1*$^{-/-}$ mice, however, more intense staining was seen in regions of disrupted RPE (Figure 8B). Analysis of the same section with isolectin B4 (Figure 8C) shows that this spot colocalizes with an RCA (Figure 8D), indicating that the abnormal blood vessels in *Cyp27a1*$^{-/-}$ retinas contain significant lipid deposits. None of these changes were observed in WT retina (Figure 8, G–J).

The overall distribution of filipin staining was similar in *Cyp27a1*$^{-/-}$ and WT animals, except in the areas of pathology. The fluorescent signal was present between the basal aspect of

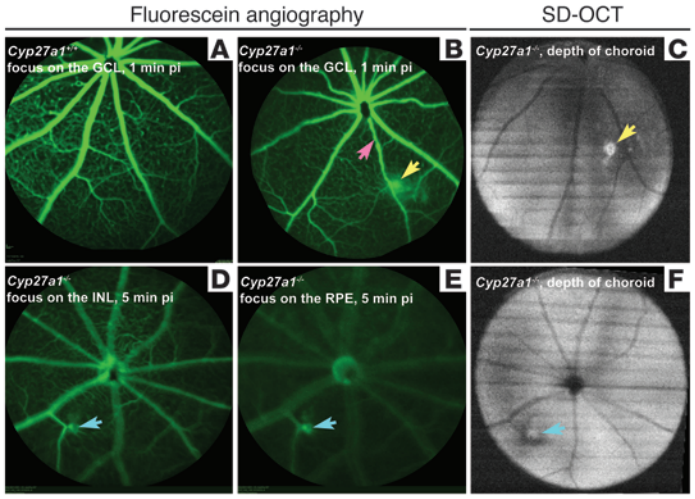

Figure 5
Leakage of blood vessels in the area of pathology in *Cyp27a1*$^{-/-}$ mice. Representative FA (55° field of view) in *Cyp27a1*$^{+/+}$ (**A**) and *Cyp27a1*$^{-/-}$ mice (**B**, **D**, and **E**). SD-OCT fundus images (50° field of view) of *Cyp27a1*$^{-/-}$ animals (**C** and **F**) are also shown. Yellow and light blue arrows point to the areas of dye leakage (**B**, **D**, and **E**) and the corresponding hyperreflective spots in OCT fundus images (**C** and **F**); arrows of the same color indicate the same animal; pink arrow points to blood vessel tortuosity and beading. pi, post injection.

the RPE and BrM in *Cyp27a1*$^{-/-}$ retinas (Figure 8, E and F) but not WT retinas (Figure 8, K and L) and was similar to that of soft drusen and basal linear deposits in AMD (54, 55). In contrast with humans, however, esterified cholesterol (EC) was not detected either in *Cyp27a1*$^{-/-}$ or WT retinas in the RPE-BrM region (data not shown).

Content of cholesterol and other sterols. We evaluated the lipid profiles of male and female retinas separately because mice are known to have sex differences in lipid and biliary homeostasis (56), and sex differences have also been observed in *Cyp27a1*$^{-/-}$ animals (37, 38). The basis of the sex difference in WT and *Cyp27a1*$^{-/-}$ mice is, however, not known. We examined a total of 10 sterols (Figure 9 and Supplemental Figure 5): cholesterol; 4 cholesterol precursors in the pathway of cholesterol biosynthesis (lanosterol, lathosterol, desmosterol, and zymosterol); 5 metabolites of cholesterol produced enzymatically (24-hydroxycholesterol, 27-hydroxycholesterol, 5-cholestenoic acid, and pregnenolone); and 1 metabolite generated nonenzymatically (7-ketocholesterol). *Cyp27a1*$^{-/-}$ mice had sex-dependent sterol-specific elevations in retinal sterol content as compared with WT animals. The levels of cholesterol, desmosterol, and 24-hydroxycholesterol were increased in at least 1 sex, whereas the concentrations of the 2 biosynthetic intermediates (lanosterol and lathosterol) and 2 cholesterol metabolites (pregnenolone and 7-ketocholesterol) were increased in both sexes. Three sterols (zymosterol, 27-hydroxycholesterol, and 5-cholestenoic acid) were below the limits of detection (<0.5 pmol/mg protein). Low steady-state levels of CYP27A1 metabolites 27-hydroxycholesterol and 5-cholestenoic acid in WT mice were consistent with a previous study detecting only subpicomolar amounts of 27-hydroxycholesterol in mouse retina (57). These levels are much lower than those in humans (28), possibly because of a much shorter death-to-tissue preservation time (<1 hour for mouse retinas and ~12 hours for human retinas) preventing sterol accumulation due to arrested blood flow. Alternatively, there may be enzymes in mouse but not human retina that act on these products, also reducing the steady-state levels of CYP27A1 metabolites in mice.

Discussion

The major findings of the present study are that *Cyp27a1*$^{-/-}$ mice have dysregulated retinal cholesterol homeostasis leading to focal depositions containing cholesterol along BrM and the development of RCAs in the lesion areas. The presence of an abnormal vascular process was implicated by fundus characterization via SD-OCT (Figure 1) and then confirmed histologically by stainings with H&E and markers for blood vessels (Figures 2–4). FA and Doppler flow of SD-OCT demonstrated blood vessel patency in vivo and revealed that the permeability of the blood vessels is increased in the areas of pathology (Figure 5) and that these areas have altered direction of blood flow and possibly reduced blood flow velocity (Figure 6). Stainings for pimonidazole and HIF-1A (Figure 7) enabled detection of decreased oxygen tensions and hypoxia in *Cyp27a1*$^{-/-}$ retina, whereas increased anti-GFAP staining suggested activation of Müller cells (Figure 4). Loss of CYP27A1 led to alteration of the retinal sterol profile (Figure 9) and slight increase in cholesterol levels either in the form of a trend in female mice or as a 1.4-fold statistically significant increase in male mice (Figure 9). Based on the data obtained, we propose a cascade of events initiated by loss of CYP27A1 (Figure 10). This cascade is putative, and alternate sequences may not be excluded.

CYP27A1 deficiency affects retinal cholesterol maintenance, which normally represents a balance between the input and output pathways: local biosynthesis and uptake from systemic circulation (23, 58–61) and elimination via lipoproteins and catabolism (10, 28, 62–65). In *Cyp27a1*$^{-/-}$ retina, cholesterol biosynthesis is increased, as indicated by increased levels of lathosterol (Figure 9), a marker of cholesterol biosynthesis (66), consistent with the knowledge that lack of CYP27A1 not only affects cholesterol biosynthesis in the liver but also in other organs, including the brain (35, 38). Upregulation of cholesterol biosynthesis in *Cyp27a1*$^{-/-}$ retinas is, however, paradoxical when this response is compared with the response of the brain to abrogation of its major pathway of cholesterol removal. Loss of Cyp46a1, controlling this pathway, was shown to lead to a compensatory reduction of cerebral cholesterol biosynthesis and unaltered levels of cerebral cholesterol (67, 68). In contrast, in the retina lacking CYP27A1, the principal retinal cholesterol hydroxylase, the response is opposite and cholesterol levels are increased up to 40% in males, indicating dysregulated retinal cholesterol maintenance. Experiments are in progress to determine whether this increase is due to a lack of hydroxylation of cholesterol precursors by CYP27A1. Our studies show that in vitro lanosterol, desmosterol, and other biosynthetic intermediates of cholesterol are efficiently metabolized by purified CYP27A1 (69).

Altered retinal cholesterol biosynthesis in *Cyp27a1*$^{-/-}$ mice is compensated for in part by the CYP11A1-mediated increase in cholesterol catabolism to pregnenolone (Figure 9), a precursor of all steroid hormones. CYP11A1 resides along with CYP27A1 in the mitochondria of cells in the GCL and INL (70–72) and likely competes with CYP27A1 for utilization of cholesterol (73). Retinal levels of 7-ketocholesterol, a product of nonenzymatic cholesterol oxidation, are also increased in *Cyp27a1*$^{-/-}$ retina, suggesting that 7-ketocholesterol is metabolized, at least in part, by CYP27A1, in agreement with our previous studies (74). 7-Ketocholesterol is of

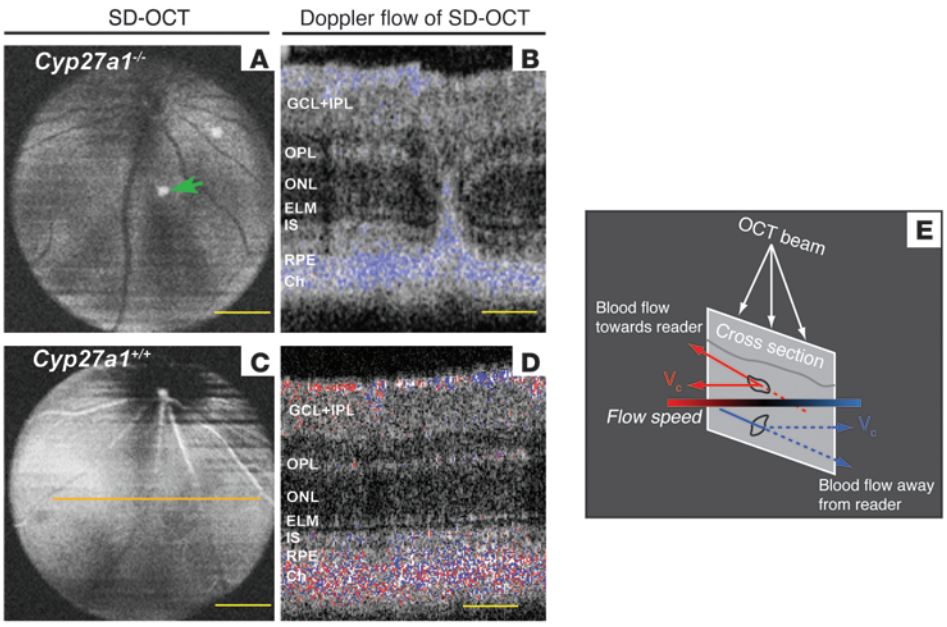

Figure 6
Doppler flow of SD-OCT shows RCA and also reveals altered direction of blood flow. (**A** and **C**) Representative OCT fundus depth images (50° field of view) at the OPL in *Cyp27a1*$^{-/-}$ and *Cyp27a1*$^{+/+}$ mice, respectively. (**B** and **D**) Doppler flow of SD-OCT cross section through pathology in **A** (indicated by green arrow) and the matching area in *Cyp27a1*$^{+/+}$ retina in **C** (indicated by orange line). Red and blue colored pixels correspond to direction and relative magnitude of the vector component of blood flow perpendicular to the plane of the scan (V_C in **E**). Areas with no flow are transparent and show the underlying SD-OCT imaging data. Scale bars: 300 μm (**A** and **C**); 60 μm (**B** and **D**).

interest because this toxic oxysterol is implicated in the pathogenesis of AMD (75). *Cyp27a1*$^{-/-}$ mice may also have changes in retinal cholesterol elimination via lipoproteins and cholesterol uptake from systemic circulation. These pathways were not investigated here but are probably affected because a significant increase in retinal cholesterol biosynthesis in *Cyp27a1*$^{-/-}$ mice is accompanied by only a small increase in retinal cholesterol.

Although cholesterol increase is small in *Cyp27a1*$^{-/-}$ retinas, it nevertheless likely leads to focal depositions containing cholesterol along BrM (Figure 8). These deposits are observed in the areas of abnormal vascularization and thus support a model for AMD wherein lipid lesions in BrM elicit choroidal NV (10, 62, 76). In addition to choroidal NV, *Cyp27a1*$^{-/-}$ mice may also have vascular processes in the retina that could be explained by an increase in retinal cholesterol biosynthesis, a highly oxygen- and energy-consuming process requiring 11 and 18 moles of O_2 and ATP, respectively, to generate 1 mole of cholesterol (77, 78). An increase in retinal cholesterol biosynthesis in *Cyp27a1*$^{-/-}$ mice may also explain retinal hypoxia and predict an overall decline in metabolic activity, a topic that we are currently exploring. In this event, hypoxia and/or other retinal insults may be responsible for Müller cell activation and may trigger retinal NV. This scheme would be consistent with the knowledge that GFAP staining is only barely detectable in normal mammalian retinas (79, 80) but is significant in AMD-affected human retinas (81). Involvement of cholesterol biosynthesis would also be consistent with the higher frequency of pathologies in *Cyp27a1*$^{-/-}$ males than females, as males had a greater elevation in the rate of cholesterol biosynthesis (2.6-fold in males vs 1.7-fold in females; Figure 9). Vascular processes in the retina and choroid of *Cyp27a1*$^{-/-}$ mice ultimately lead to RCA. Thus, by analysis of *Cyp27a1*$^{-/-}$ mice as a model for studies of the putative link between cholesterol and AMD, we obtained data supporting this link as well as mechanistic insights into the processes underlying this link.

The formation of RCAs was first reported in mice lacking the receptor for very low-density lipoprotein (VLDLR) (82). In these animals, abnormal blood vessels originate from the deep capillary bed of the retina and extend unidirectionally toward the RPE. In contrast, in *Cyp27a1*$^{-/-}$ mice, NV seems to occur in both the retina and choroid. The retinal phenotype of *Vldlr*$^{-/-}$ mice is also more severe than that of *Cyp27a1*$^{-/-}$ animals, with a greater incidence of RCA and FA leakage as well as photoreceptor degeneration and reduced ERG amplitudes (82–84). In *Cyp27a1*$^{-/-}$ mice, focal photoreceptor degeneration occurred only in areas of RCA formation, and the retina otherwise retained a normal appearance and function (Supplemental Figure 3). Different manifestations of RAP in *Vldlr*$^{-/-}$ and *Cyp27a1*$^{-/-}$ mice suggest different variants of the vasogenic process. Focal retinal proliferation and progression is observed in retinas lacking VLDLR, while focal retinal proliferation with preexisting or simultaneous choroidal proliferation is probably seen in mice lacking CYP27A1 (Figure 1, B–D). The availability of *Vldlr*$^{-/-}$ mice allows the angiogenic sequences to be carefully studied and experimental treatments evaluated (84–88). Despite these advances, our opportunities to study focal retinal proliferation with preexisting or simultaneous choroidal proliferation are currently limited. We suggest that *Cyp27a1*$^{-/-}$ mice will be useful in characterizing this variant of RAP. Since standard rodent chow contains very little fat and cholesterol, as compared with human diets, we are assessing whether a high-fat and cholesterol-rich diet leads to a more severe retinal phenotype in *Cyp27a1*$^{-/-}$ mice. With respect to treatment strategies of RAP, they may be variant specific. If so, the present work suggests that systemic administration of a statin that penetrates the blood-retina barrier and suppresses retinal cholesterol biosynthesis could also suppress the progression of RAPs observed in *Cyp27a1*$^{-/-}$ mice. The standard treatment for CTX is replacement therapy with chenodeoxycholic acid either alone or in combination with a statin. These pharmacologic interventions are known to improve general clinical symptoms, but it has not yet been studied whether they improve ophthalmic manifestations of CTX.

VLDLR and CYP27A1 play different roles in lipid and cholesterol metabolism. VLDLR is a receptor for the lipid transporter, whereas CYP27A1 is a catabolic enzyme. Loss of either protein leads to retinal NV and RAP formation, indicating that

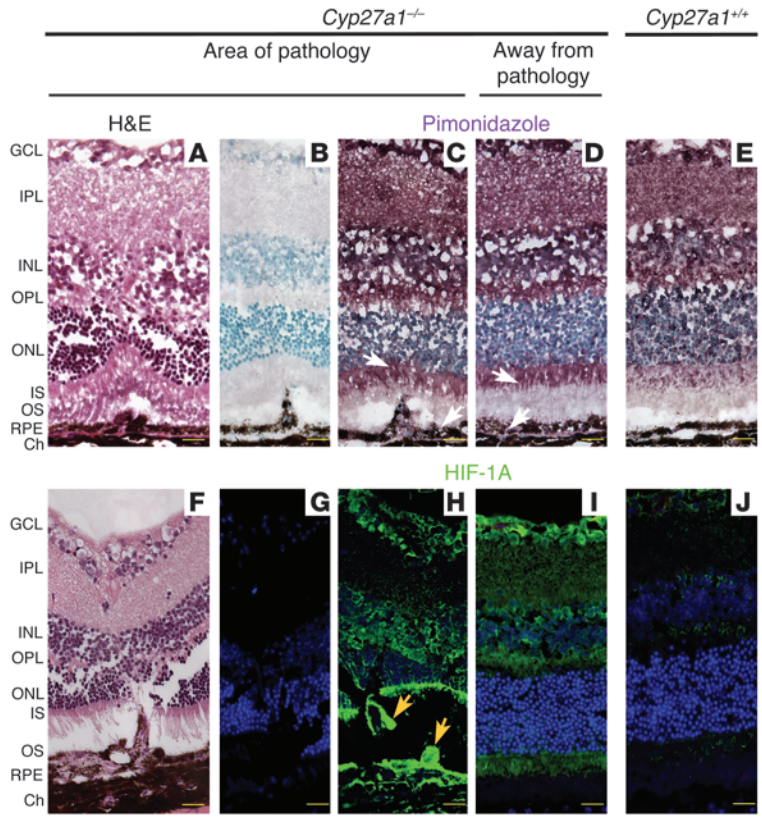

Figure 7
Retinal hypoxia in *Cyp27a1*$^{-/-}$ mice. Representative H&E (**A** and **F**), anti-pimonidazole (in dark purple, **C**–**E**), and anti-HIF1A stainings (in green, **H**–**J**) of *Cyp27a1*$^{-/-}$ and *Cyp27a1*$^{+/+}$ mice. (**B** and **G**) Negative controls treated with serum from nonimmunized animal. White arrows (**C** and **D**) indicate increased staining intensity relative to *Cyp27a1*$^{+/+}$ (**E**), and gold arrows (**H**) indicate intense staining in the blood vessel above BrM. For fluorescence imaging, nuclei were stained with DAPI (in blue), and immunoreactivity was detected by DyLight 649–conjugated fluorophore (in green). For pimonidazole adducts, immunoreactivity was detected by the ImmPACT VIP Peroxidase Substrate (in dark purple) and nuclei were stained with methyl green. Scale bars: 30 μm. Original magnification, ×400.

the triggering events overlap. One of them could be reduced expression of VLDLR in *Cyp27a1*$^{-/-}$ mice (Supplemental Figure 6). Indeed, studies in cell culture and mice show that the transcription of *Vldlr* is induced by the farnesoid X receptor (FXR), which is activated by bile acids (89). The pool of bile acids is reduced in *Cyp27a1*$^{-/-}$ mice (34, 37); therefore retinal expression of VLDLR could be reduced as well. The caveat is that we do not know whether the FXR-dependent mechanism is operative in the retina, i.e., whether FXR and its mediating partner small heterodimer protein (SHP) are expressed and localized to the same cell types that express VLDLR (90). Moreover, the expression of FXR and SHP was not altered in the liver of *Cyp27a1*$^{-/-}$ mice, suggesting that the reduction in the bile acid pool was not sufficient to affect the FXR-mediated regulation of the target genes in this organ (37). In human and mouse cell cultures and mice, protein levels of VLDLR are also sensitive to cellular content of the E3 ubiquitin ligase inducible degrader of the low-density lipoprotein receptor (IDOL), which induces degradation of VLDLR (91). The transcription of *IDOL* is regulated by the liver X receptor (LXR), activated in turn by a number of oxysterols, including the CYP27A1 products 27-hydroxycholesterol and 5-cholestenoic acid (92, 93). Although the latter 2 are not detected in mouse retina, in *Cyp27a1*$^{-/-}$ animals, there may be an increase in the retinal concentrations of other Lxr ligands, such as 24,25-epoxycholesterol and follicular fluid meiosis-activating sterol, generated in the shunt and branch pathways of cholesterol biosynthesis, respectively (92, 94). Increased concentration of these sterols would activate LXR and induce the degradation of VLDLR via the LXR-mediated upregulation of IDOL. A reduced expression of VLDLR is thus possible in *Cyp27a1*$^{-/-}$ retina and could explain both RAP and the diminished severity of symptoms in these mice as compared with *Vldlr*$^{-/-}$ mice. Yet this hypothetical scenario requires experimental support. While overlapping, etiologic factors for NV are probably not identical in *Vldlr*$^{-/-}$ and *Cyp27a1*$^{-/-}$ mice; hence, their retinal phenotypes represent distinct variants of RAP.

In summary, by performing a comprehensive ophthalmic characterization of mice deficient in CYP27A1, a multifunctional enzyme involved in metabolism of various lipids, we discovered RCA putatively arising from simultaneous focal proliferations in the choroid and retina. We also observed an increase in overall retinal cholesterol biosynthesis and in the production of steroid hormones; depositions containing cholesterol in the areas of pathology; and altered blood flow, hypoxia, and activation of Müller cells. We propose an explanation for how all these retinal abnormalities relate to each other and are linked to dysregulated cholesterol homeostasis. We also suggest that *Cyp27a1*$^{-/-}$ mice can serve as a model for studies of one of the variants of type 3 retinal NV and thus expand our understanding of the mechanisms underlying retinal NV and provide a means for evaluating therapeutic options for the treatment of this abnormality. Collectively, our findings indicate the importance of enzymatic cholesterol metabolism for maintenance of retinal structure and function.

Methods

Animals. *Cyp27a1*$^{+/-}$ mice were obtained from the laboratory of Sandra Erickson (UCSF, San Francisco, California, USA) (37) and were used to breed the *Cyp27a1*$^{-/-}$ and WT littermates studied here. Mice were maintained on a standard 12-hour light/12-hour dark (with light less than 10 lux) cycle and were fed standard rodent chow and water ad libitum.

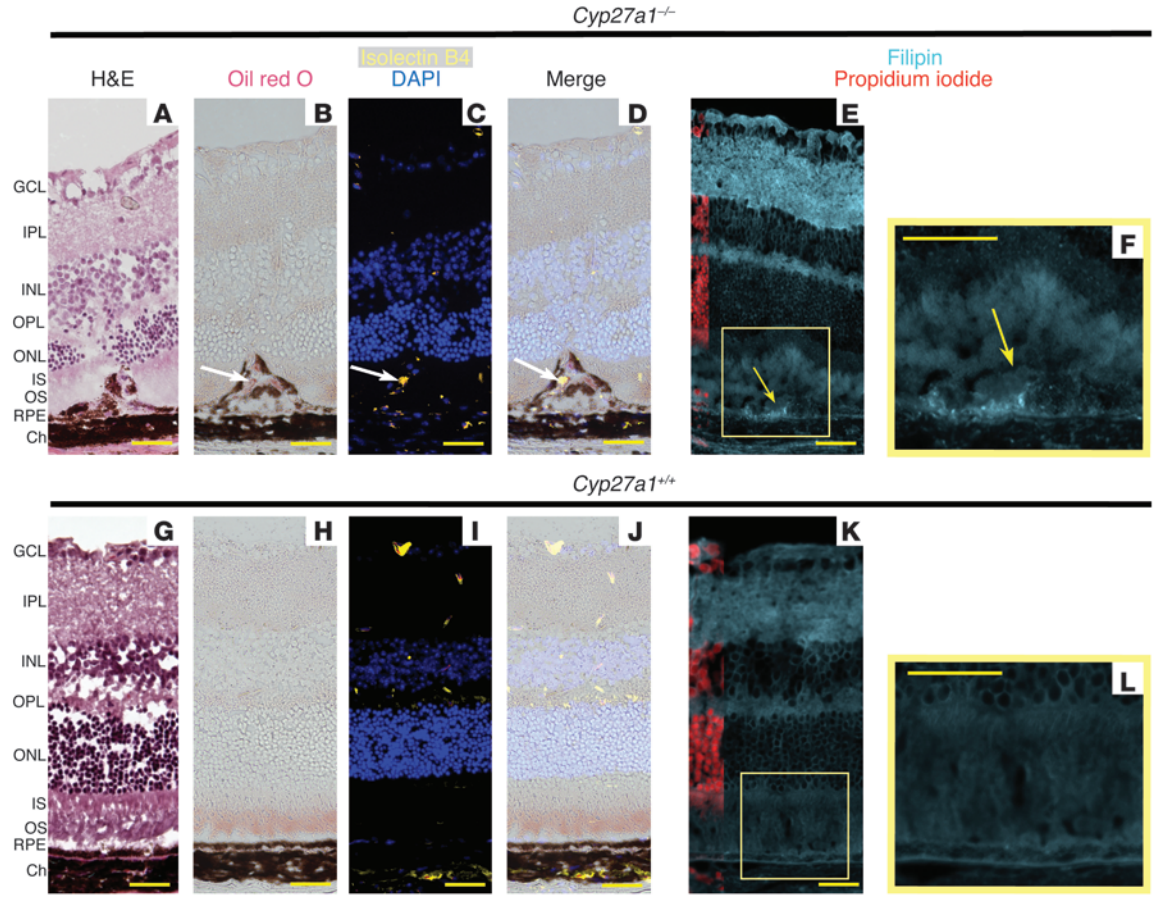

Figure 8
Lipid and cholesterol deposition beneath the RPE in *Cyp27a1*$^{-/-}$ mice. Panels are representative of stainings carried out on adjacent sections cut through pathologies in *Cyp27a1*$^{-/-}$ mice (**A**–**F**) or through corresponding regions in *Cyp27a1*$^{+/+}$ mice (**G**–**L**). (**A** and **G**) H&E staining. (**B** and **H**) Localizations of neutral lipids with oil red O (in fuchsia). (**C** and **I**) Staining with blood-vessel marker isolectin B4 conjugated to DyLight 594 fluorophore (in yellow); nuclei were stained with DAPI (in blue). (**D** and **J**) Merger of **B** and **C** and **H** and **I**, respectively. White arrows (**B**–**D**) indicate colocalized staining. (**E** and **K**) Detection of UC with filipin (in cyan); nuclei were stained with propidium iodide (in red). (**F** and **L**) Enlarged regions of **E** and **K**, respectively. Scale bars: 30 μm. Original magnification, ×400.

SD-OCT. In vivo imaging of mouse retinas was carried out using 840HHP SD-OCT (Bioptigen). Mice were anesthetized via intraperitoneal injection of 80 mg/kg ketamine (Fort Dodge Animal Health) and 15 mg/kg xylazine (Akorn Inc.) in PBS, pH 7.4, and pupils dilated with 1% tropicamide drops (Bausch & Lomb). Mice were placed on a freely rotating cassette to align the eye with the imaging probe. Lubricating drops (Tears Naturale II; Alcon Laboratories Inc.) were instilled on both eyes to minimize corneal drying. En face OCT fundus data were acquired with the following parameters: 1.6 mm × 1.6 mm scan area, 350 A-scans per B-scan, and 350 B-scans. Fundus depth images were created after acquisition by aligning B-scans in a horizontal direction and selecting the range of depth through the retinal layers of interest. Cross-sectional images are averages of 40 B-scans (1200 A-scans per B-scan). Labeling of the hyperreflective bands in the outer retina was according to a previous study (95).

FA. Mice were anesthetized and eyes dilated as above. A 0.10-ml bolus of 1.6% sodium fluorescein in PBS was injected intraperitoneally. Retina monitoring started 1 minute after injection and continued for 10 minutes. Images were acquired every 2 minutes using a scanning laser ophthalmoscope (Spectralis HRA+OCT; Heidelberg Engineering) in the short-wavelength autofluorescence mode.

Specimen preparation for light microscopy. Following animal sacrifice, inferior corneas were marked with tissue marker or burn mark to preserve orientation after enucleation and during embedding. For cryosectioning, eyes were enucleated and placed in 4% PFA for 3 hours and then transferred to 1% PFA and incubated overnight. These were then processed and embedded in OCT medium (Tissue-Tek) and stored at –80°C until cut. For paraffin sections, enucleated eyes were placed in 4% PFA for 18 hours and then sequentially transferred to PBS and embedded. Sections (5-μm thick) were cut, deparaffinized, stained with hematoxylin (Gill's Formulation #2; Fisher Scientific) and eosin (alcoholic eosin Y; Fisher Scientific) and viewed with an inverted microscope (DMI 6000 B; Leica Microsystems) in the brightfield mode.

Immunohistochemistry. Frozen sections (5-μm thick) were air-dried for 30 minutes, washed in cold acetone for 10 minutes, and then washed several times with PBS. The sections were blocked with 5% goat serum and 0.05% Tween 20 in PBS. Sections were incubated with primary antibodies diluted in blocking buffer overnight at 4°C. Then the sections were washed with PBS and incubated for 1 hour with secondary antibodies diluted with blocking buffer. Slides were rinsed in PBS with 0.05% Tween 20, then rinsed in distilled water and mounted with Prolong Gold

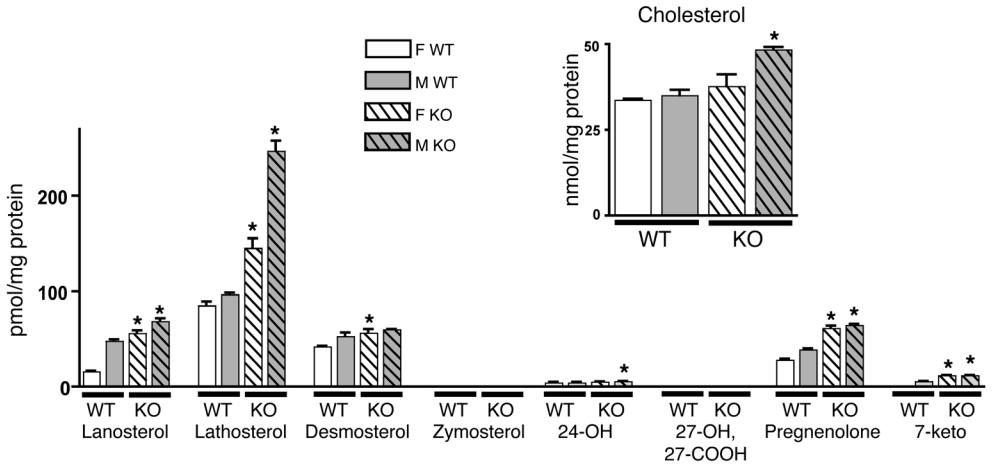

Figure 9
Retinal sterol profile is altered in *Cyp27a1*$^{-/-}$ mice. Open and dashed bars show concentrations of sterols in WT and *Cyp27a1*$^{-/-}$ animals, respectively; white bars, females (F) and gray bars, males (M). Retinas from 40 animals per group were pooled. 24-OH, 24S-hydroxycholesterol; 27-OH, 27-hydroxycholesterol; 27-COOH, 5-cholestenoic acid; 7-keto, 7-ketocholesterol. *$P < 0.05$, compared with age- and sex-matched WT littermates.

containing DAPI (Invitrogen) for nuclear staining and viewed using an inverted fluorescence microscope. For paraffin sections, heat-induced antigen retrieval in sodium citrate buffer, pH 6.0, was performed for 20 minutes prior to washes and incubation with primary antibody. The dilutions of primary antibodies/lectins were 1:1,000 for rabbit anti-GS (Abcam), 1:100 for rabbit anti–HIF-1A (Novus Biologicals), 1:4,000 for chicken GFAP (Pierce), 1:100 for *Lycopersicon esculentum* tomato lectin (Vector Laboratories), and 1:100 for Isolectin B4 (Vector Laboratories). The secondary antibodies were goat anti-rabbit DyLight 649 and DyLight 488 diluted 1:200 and goat anti-chicken DyLight 649 diluted 1:1,000 (Jackson Inc.).

Immunohistochemistry for hypoxia marker pimonidazole. Live mice were injected intraperitoneally with 60 mg/kg pimonidazole hydrochloride in PBS (Hypoxyprobe-1 Plus Kit; Chemicon International) and sacrificed 1 hour later. Eyes were enucleated and cryosectioned. Sections were washed in PBS and then with 3% hydrogen peroxide in PBS for 5 minutes to quench endogenous peroxidase activity. Then sections were blocked with 5% rabbit serum in PBS with 0.05% Tween 20 for 1 hour (Sigma-Aldrich) and incubated with FITC-conjugated anti-pimonidazole primary antibody at 1:50 dilution (Chemicon International) overnight at 4°C. Sections were washed 3 times with PBS and incubated with horseradish peroxidase–conjugated rabbit anti-FITC secondary antibody at 1:100 dilution, followed by 3 washes in PBS and incubation with peroxidase substrate solution (ImmPACT VIP Peroxidase Substrate; Vector Laboratories) for 3 minutes. Nuclei were counterstained with Methyl Green (Newcomer Supply Inc.) for 2 minutes. Slides were washed with distilled water and mounted with Dako Glycergel Aqueous Mounting Medium (Dako Inc.). Slides were viewed on an inverted microscope in the brightfield mode.

Histochemistry for neutral lipids. Cryosections for oil red O staining were equilibrated to room temperature for 30 minutes and washed with distilled water. Sections were treated with 0.03% oil red O in water (prepared from 0.6% stock in isopropanol) for 10 minutes, followed by 3 washes in water. Slides were mounted with Dako Glycergel Aqueous Mounting Medium and viewed on the inverted microscope in the brightfield mode.

Histochemistry with filipin. Sections were removed from the freezer, equilibrated to room temperature for 30 minutes, and washed with PBS 3 times for 5 minutes. To detect UC, filipin III (Cayman Chemical), 0.083 mg/ml in PBS prepared from a 3.3 mg/ml stock in DMSO, was applied to slides for 1 hour in the dark. Slides were then rinsed 3 times with PBS and coverslipped with Vectashield mounting medium containing propidium iodide (Vector Laboratories Inc.). Detection of EC required 2 additional steps prior to filipin treatment: extraction of UC with 70% ethanol for 10 minutes and hydrolysis of EC by cholesterol esterase (15 mg/ml in 0.1 M KP_i, pH 7.2; Sigma-Aldrich) for 3.5 hours at 37°C followed by the three 5-minute washes with PBS. Filipin fluorescence was excited at 340–380 nm and emission collected at 385–470 nm. The excitation and emission wavelengths for the propidium iodide detection were 535 nm and 615 nm, respectively.

Quantification of sterols in the retina. Retinas from 40 animals of the same sex and genotype were pooled and analyzed in triplicate for sterol content by isotope dilution gas chromatography–mass spectrometry as described (28, 74). Only unesterified forms of sterols were quantified because pregnenolone and 7-ketocholesterol significantly decompose during saponification. The following ions (m/z) were monitored in the specific ion monitoring mode: 368 (cholesterol) and 375 ([$^2H_7$]cholesterol); 145 (24-hydroxycholesterol) and 152 ([$^2H_7$]24-hydroxycholesterol); 417 (27-hydroxycholesterol) and 422 ([$^2H_5$]27-hydroxycholesterol); 388 (pregnenolone) and 392 ([$^2H_4$]pregnenolone); 331 (cholenic acid) and 373 and 412 (5-cholestenoic acid); 458 (lathos-

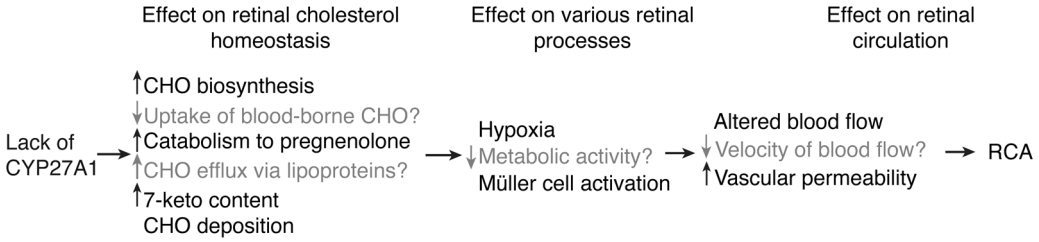

Figure 10
Putative cascade of events initiated by CYP27A1 deficiency in the retina. Events within columns may occur in parallel or in different order. Events in gray type are putative and have not yet been confirmed experimentally. CHO, cholesterol.

terol) and 462 ([$^2H_4$]lathosterol; 393 (lanosterol) and 399 ([$^2H_6$]lanosterol); 366 (desmosterol) and 372 ([$^2H_6$]desmosterol); 456 zymosterol and 461 ([$^2H_5$]zymosterol), 472 (7-ketocholesterol) and 479 ([$^2H_7$]7-ketocholesterol).

ERG. After overnight dark adaptation, mice were anesthetized and pupils were dilated as mentioned above. A contact lens electrode was then placed on each cornea and reference and ground electrodes were placed in the scalp and tail, respectively. ERGs were recorded using Universal Testing and Electrophysiological System UTAS E-3000 (LKC Technologies Inc.). White light flash stimuli intensity ranged from –3.7 to 2.1 log cd•s/m^2. From 3 to 5 responses were averaged at each stimulus level, and interstimulus levels were at least 10 seconds in duration and up to 1 minute for the highest flash stimuli. Photopic, cone-mediated ERGs were recorded in response to strobe stimuli superimposed upon a steady background light (150 cd/m^2) after 7 minutes of light adaptation. The amplitude of the a-wave was measured at 7 msec after flash presentation from the prestimulus baseline. The b-wave amplitude was measured from the a-wave minimum to the b-wave maximum.

Statistics. All data represent mean ± SD. A 2-tailed, unpaired Student's *t* test was used to determine statistical significance in sterol quantification experiments, and one-way ANOVA (SAS Institute Inc.) was used to analyze the ERG data. In all statistical analyses, *P* values of less than 0.05 were considered significant.

Study approval. All animal procedures were approved by the Case Western Reserve University Institutional Animal Care and Use Committee and conformed to recommendations of the American Veterinary Association Panel on Euthanasia and the Association for Research in Vision and Ophthalmology.

Acknowledgments

The authors thank the Visual Sciences Research Center Core Facility (supported by P30 EY11373) for assistance with genotyping (Anna Yakubenko), tissue sectioning (Cathy Doller), and microscopy (Scott Howell). Many thanks to Timothy Kern and Alex Veenstra for help with FA techniques. This work was supported in part by grants from the NIH (EY018383 to I.A. Pikuleva), predoctoral and postdoctoral research training fellowships T32 EY07157 from the Visual Sciences Training Program (to C.D. Charvet and R.E. Reem, respectively), funds from the Veterans Administration Office of Research and Development (to N.S. Peachey), the Ohio Lions Eye Research Foundation, and the Foundation Fighting Blindness, and unrestricted grants from Research to Prevent Blindness. I.A. Pikuleva is a recipient of the Jules and Doris Stein Professorship from Research to Prevent Blindness.

Received for publication March 12, 2012, and accepted in revised form May 24, 2012.

Address correspondence to: Irina A. Pikuleva, Department of Ophthalmology and Visual Sciences, Case Western Reserve University, 2085 Adelbert Rd., r. 303a, Cleveland, Ohio 44106, USA. Phone: 216.368.3823; Fax: 216.360.3482; E-mail: iap8@case.edu.

Rachel E. Reem's present address is: Havener Eye Institute, Ohio State University, Columbus, Ohio, USA.

1. Pascolini D, et al. 2002 global update of available data on visual impairment: a compilation of population-based prevalence studies. *Ophthalmic Epidemiol*. 2004;11(2):67–115.
2. Gass JD. *Atlas of Macular Diseases.* St. Louis, Missouri, USA: CV Mosby; 1997.
3. Yannuzzi LA, Freund KB, Takahashi BS. Review of retinal angiomatous proliferation or type 3 neovascularization. *Retina*. 2008;28(3):375–384.
4. Strauss O. The retinal pigment epithelium in visual function. *Physiol Rev*. 2005;85(3):845–881.
5. Ghazi NG. Retinal angiomatous proliferation in age-related macular degeneration. *Retina*. 2002; 22(4):509–511.
6. de Jong PT. Age-related macular degeneration. *N Engl J Med*. 2006;355(14):1474–1485.
7. Ding X, Patel M, Chan CC. Molecular pathology of age-related macular degeneration. *Prog Retin Eye Res*. 2009;28(1):1–18.
8. Abdelsalam A, Del Priore L, Zarbin MA. Drusen in age-related macular degeneration: pathogenesis, natural course, and laser photocoagulation-induced regression. *Surv Ophthalmol*. 1999;44(1):1–29.
9. Sarks SH, Arnold JJ, Killingsworth MC, Sarks JP. Early drusen formation in the normal and aging eye and their relation to age related maculopathy: a clinicopathological study. *Br J Ophthalmol*. 1999;83(3):358–368.
10. Curcio CA, Johnson M, Rudolf M, Huang JD. The oil spill in ageing Bruch membrane. *Br J Ophthalmol*. 2011;95(12):1638–1645.
11. Malek G, Li CM, Guidry C, Medeiros NE, Curcio CA. Apolipoprotein B in cholesterol-containing drusen and basal deposits of human eyes with age-related maculopathy. *Am J Pathol*. 2003;162(2):413–425.
12. Wang L, et al. Abundant lipid and protein components of drusen. *PLoS One*. 2010;5(4):e10329.
13. Klaver CC, et al. Incidence and progression rates of age-related maculopathy: the Rotterdam Study. *Invest Ophthalmol Vis Sci*. 2001;42(10):2237–2241.
14. Mitchell P, Wang JJ, Foran S, Smith W. Five-year incidence of age-related maculopathy lesions: the Blue Mountains Eye Study. *Ophthalmology*. 2002;109(6):1092–1097.
15. Klein R, Klein BE, Tomany SC, Cruickshanks KJ. The association of cardiovascular disease with the long-term incidence of age-related maculopathy: the Beaver Dam eye study. *Ophthalmology*. 2003;110(4):636–643.
16. Tomany SC, et al. Risk factors for incident age-related macular degeneration: pooled findings from 3 continents. *Ophthalmology*. 2004;111(7):1280–1287.
17. van Leeuwen R, et al. Cholesterol and age-related macular degeneration: is there a link? *Am J Ophthalmol*. 2004;137(4):750–752.
18. Souied EH, et al. The epsilon4 allele of the apolipoprotein E gene as a potential protective factor for exudative age-related macular degeneration. *Am J Ophthalmol*. 1998;125(3):353–359.
19. Klaver CC, et al. Genetic association of apolipoprotein E with age-related macular degeneration. *Am J Hum Genet*. 1998;63(1):200–206.
20. Neale BM, et al. Genome-wide association study of advanced age-related macular degeneration identifies a role of the hepatic lipase gene (LIPC). *Proc Natl Acad Sci U S A*. 2010;107(16):7395–7400.
21. Chen W, et al. Genetic variants near TIMP3 and high-density lipoprotein-associated loci influence susceptibility to age-related macular degeneration. *Proc Natl Acad Sci U S A*. 2010;107(16):7401–7406.
22. Yu Y, Reynolds R, Rosner B, Daly MJ, Seddon JM. Prospective assessment of genetic effects on progression to different stages of age-related macular degeneration using multi-state markov models. *Invest Ophthalmol Vis Sci*. 2012;53(3):1548–1556.
23. Fliesler SJ, Bretillon L. The ins and outs of cholesterol in the vertebrate retina. *J Lipid Res*. 2010;51(12):3399–3413.
24. Edwards AO, Malek G. Molecular genetics of AMD and current animal models. *Angiogenesis*. 2007; 10(2):119–132.
25. Zeiss CJ. Animals as models of age-related macular degeneration: an imperfect measure of the truth. *Vet Pathol*. 2010;47(3):396–413.
26. Pikuleva IA. Cytochrome P450s and cholesterol homeostasis. *Pharmacol Ther*. 2006;112(3):761–773.
27. Liao WL, et al. Quantification of cholesterol-metabolizing P450s CYP27A1 and CYP46A1 in neural tissues reveals a lack of enzyme-product correlations in human retina but not human brain. *J Proteome Res*. 2011;10(1):241–248.
28. Mast N, et al. Cholestenoic acid is an important elimination product of cholesterol in the retina: comparison of retinal cholesterol metabolism to that in the brain. *Invest Ophthalmol Vis Sci*. 2011; 52(1):594–603.
29. Bjorkhem I, Boberg KM, Leitersdorf E. Inborn errors in bile acid biosynthesis and storage of sterols other than cholesterol. In: Scriver AL, Beaudet AL, Sly WS, Valle D, Childs B, eds. *The Metabolic And Molecular Bases Of Inherited Disease*. New York, New York, USA: McGraw–Hill; 1995:2073–2099.
30. Bjorkhem I, Hansson M. Cerebrotendinous xanthomatosis: an inborn error in bile acid synthesis with defined mutations but still a challenge. *Biochem Biophys Res Commun*. 2010;396(1):46–49.
31. Cruysberg JR, Wevers RA, van Engelen BG, Pinckers A, van Spreeken A, Tolboom JJ. Ocular and systemic manifestations of cerebrotendinous xanthomatosis. *Am J Ophthalmol*. 1995;120(5):597–604.
32. Morgan SJ, McKenna P, Bosanquet RC. Case of cerebrotendinous xanthomatosis. I: Unusual ophthalmic features. *Br J Ophthalmol*. 1989; 73(12):1011–1014.
33. Dotti MT, Rufa A, Federico A. Cerebrotendinous xanthomatosis: heterogeneity of clinical phenotype with evidence of previously undescribed ophthalmological findings. *J Inherit Metab Dis*. 2001; 24(7):696–706.
34. Rosen H, et al. Markedly reduced bile acid synthesis but maintained levels of cholesterol and vitamin D metabolites in mice with disrupted sterol 27-hydroxylase gene. *J Biol Chem*. 1998; 273(24):14805–14812.
35. Repa JJ, et al. Disruption of the sterol 27-hydroxylase gene in mice results in hepatomegaly and hypertriglyceridemia. Reversal by cholic acid feeding. *J Biol Chem*. 2000;275(50):39685–39692.
36. Honda A, et al. Differences in hepatic levels of inter-

mediates in bile acid biosynthesis between Cyp27(–/–) mice and CTX. *J Lipid Res*. 2001;42(2):291–300.
37. Dubrac S, et al. Role of CYP27A in cholesterol and bile acid metabolism. *J Lipid Res*. 2005;46(1):76–85.
38. Bavner A, et al. On the mechanism of accumulation of cholestanol in the brain of mice with a disruption of sterol 27-hydroxylase. *J Lipid Res*. 2010; 51(9):2722–2730.
39. Coscas F, Coscas G, Souied E, Tick S, Soubrane G. Optical coherence tomography identification of occult choroidal neovascularization in age-related macular degeneration. *Am J Ophthalmol*. 2007; 144(4):592–599.
40. Campos M, Amaral J, Becerra SP, Fariss RN. A novel imaging technique for experimental choroidal neovascularization. *Invest Ophthalmol Vis Sci*. 2006;47(12):5163–5170.
41. Lin M, et al. Ischaemia-induced retinal neovascularisation and diabetic retinopathy in mice with conditional knockout of hypoxia-inducible factor-1 in retinal Muller cells. *Diabetologia*. 2011;54(6):1554–1566.
42. Loewen N, Chen J, Dudley VJ, Sarthy VP, Mathura JR Jr. Genomic response of hypoxic Muller cells involves the very low density lipoprotein receptor as part of an angiogenic network. *Exp Eye Res*. 2009;88(5):928–937.
43. Shen X, Zhong Y, Xie B, Cheng Y, Jiao Q. Pigment epithelium derived factor as an anti-inflammatory factor against decrease of glutamine synthetase expression in retinal Muller cells under high glucose conditions. *Graefes Arch Clin Exp Ophthalmol*. 2010;248(8):1127–1136.
44. Kuzmanovic M, Dudley VJ, Sarthy VP. GFAP promoter drives Muller cell-specific expression in transgenic mice. *Invest Ophthalmol Vis Sci*. 2003; 44(8):3606–3613.
45. Wu KH, Madigan MC, Billson FA, Penfold PL. Differential expression of GFAP in early v late AMD: a quantitative analysis. *Br J Ophthalmol*. 2003; 87(9):1159–1166.
46. Querques G, Avellis FO, Querques L, Massamba N, Bandello F, Souied EH. Three dimensional spectral domain optical coherence tomography features of retinal-choroidal anastomosis. *Graefes Arch Clin Exp Ophthalmol*. 2011;250(2):165–173.
47. Stefansson E, Geirsdottir A, Sigurdsson H. Metabolic physiology in age related macular degeneration. *Prog Retin Eye Res*. 2010;30(1):72–80.
48. Varia MA, et al. Pimonidazole: a novel hypoxia marker for complementary study of tumor hypoxia and cell proliferation in cervical carcinoma. *Gynecol Oncol*. 1998;71(2):270–277.
49. Jiang BH, Semenza GL, Bauer C, Marti HH. Hypoxia-inducible factor 1 levels vary exponentially over a physiologically relevant range of O2 tension. *Am JPhysiol*. 1996;271(4 pt 1):C1172–1180.
50. Kizaka-Kondoh S, Tanaka S, Harada H, Hiraoka M. The HIF-1-active microenvironment: an environmental target for cancer therapy. *Adv Drug Deliv Rev*. 2009;61(7–8):623–632.
51. Jankovic B, et al. Comparison between pimonidazole binding, oxygen electrode measurements, and expression of endogenous hypoxia markers in cancer of the uterine cervix. *Cytometry B Clin Cytom*. 2006;70(2):45–55.
52. Sobhanifar S, Aquino-Parsons C, Stanbridge EJ, Olive P. Reduced expression of hypoxia-inducible factor-1alpha in perinecrotic regions of solid tumors. *Cancer Res*. 2005;65(16):7259–7266.
53. Castanho MA, Coutinho A, Prieto MJ. Absorption and fluorescence spectra of polyene antibiotics in the presence of cholesterol. *J Biol Chem*. 1992; 267(1):204–209.
54. Curcio CA, Presley JB, Malek G, Medeiros NE, Avery DV, Kruth HS. Esterified and unesterified cholesterol in drusen and basal deposits of eyes with age-related maculopathy. *Exp Eye Res*. 2005; 81(6):731–741.
55. Curcio CA, Millican CL, Bailey T, Kruth HS. Accumulation of cholesterol with age in human Bruch's membrane. *Invest Ophthalmol Vis Sci*. 2001; 42(1):265–274.
56. Turley SD, Schwarz M, Spady DK, Dietschy JM. Gender-related differences in bile acid and sterol metabolism in outbred CD-1 mice fed low- and high-cholesterol diets. *Hepatology*. 1998; 28(4):1088–1094.
57. Bojanic DD, et al. Differential expression and function of ABCG1 and ABCG4 during development and aging. *J Lipid Res*. 2010;51(1):169–181.
58. Tserentsoodol N, et al. Uptake of cholesterol by the retina occurs primarily via a low density lipoprotein receptor-mediated process. *Mol Vis*. 2006; 12:1306–1318.
59. Fliesler SJ, Florman R, Rapp LM, Pittler SJ, Keller RK. In vivo biosynthesis of cholesterol in the rat retina. *FEBS Lett*. 1993;335(2):234–238.
60. Fliesler SJ, Keller RK. Isoprenoid metabolism in the vertebrate retina. *Int J Biochem Cell Biol*. 1997; 29(6):877–894.
61. Elner VM. Retinal pigment epithelial acid lipase activity and lipoprotein receptors: effects of dietary omega-3 fatty acids. *Trans Am Ophthalmol Soc*. 2002; 100:301–338.
62. Curcio CA, Johnson M, Huang JD, Rudolf M. Apolipoprotein B-containing lipoproteins in retinal aging and age-related macular degeneration. *J Lipid Res*. 2010;51(3):451–467.
63. Tserentsoodol N, Gordiyenko NV, Pascual I, Lee JW, Fliesler SJ, Rodriguez IR. Intraretinal lipid transport is dependent on high density lipoprotein-like particles and class B scavenger receptors. *Mol Vis*. 2006;12:1319–1333.
64. Bretillon L, et al. Cholesterol-24S-hydroxylase (CYP46A1) is specifically expressed in neurons of the neural retina. *Curr Eye Res*. 2007;32(4):361–366.
65. Ramirez DM, Andersson S, Russell DW. Neuronal expression and subcellular localization of cholesterol 24-hydroxylase in the mouse brain. *J Comp Neurol*. 2008;507(5):1676–1693.
66. Lund E, Sisfontes L, Reihner E, Bjorkhem I. Determination of serum levels of unesterified lathosterol by isotope dilution-mass spectrometry. *Scand J Clin Lab Invest*. 1989;49(2):165–171.
67. Kotti TJ, Ramirez DM, Pfeiffer BE, Huber KM, Russell DW. Brain cholesterol turnover required for geranylgeraniol production and learning in mice. *Proc Natl Acad Sci U S A*. 2006;103(10):3869–3874.
68. Russell DW, Halford RW, Ramirez DM, Shah R, Kotti T. Cholesterol 24-hydroxylase: an enzyme of cholesterol turnover in the brain. *Annu Rev Biochem*. 2009;78:1017–1040.
69. Pikuleva I, Javitt NB. Novel sterols synthesized via the CYP27A1 metabolic pathway. *Arch Biochem Biophys*. 2003;420(1):35–39.
70. Guarneri P, Guarneri R, Cascio C, Pavasant P, Piccoli F, Papadopoulos V. Neurosteroidogenesis in rat retinas. *J Neurochem*. 1994;63(1):86–96.
71. Jaliffa CO, et al. Effect of neurosteroids on the retinal gabaergic system and electroretinographic activity in the golden hamster. *J Neurochem*. 2005; 94(6):1666–1675.
72. Lee JW, Fuda H, Javitt NB, Strott CA, Rodriguez IR. Expression and localization of sterol 27-hydroxylase (CYP27A1) in monkey retina. *Exp Eye Res*. 2006; 83(2):465–469.
73. Heo GY, Liao WL, Turko IV, Pikuleva IA. Features of the retinal environment which affect the activities and product profile of cholesterol-metabolizing cytochromes P450 CYP27A1 and CYP11A1. *Arch Biochem Biophys*. 2012;518(2):119–126.
74. Heo GY, Bederman I, Mast N, Liao WL, Turko IV, Pikuleva IA. Conversion of 7-ketocholesterol to oxysterol metabolites by recombinant CYP27A1 and retinal pigment epithelial cells. *J Lipid Res*. 2011; 52(6):1117–1127.
75. Rodriguez IR, Larrayoz IM. Cholesterol oxidation in the retina: Implications of 7-ketocholesterol formation in chronic inflammation and age-related macular degeneration. *J Lipid Res*. 2010;51(10):2847–2862.
76. Curcio CA, Johnson M, Huang JD, Rudolf M. Aging, age-related macular degeneration, and the response-to-retention of apolipoprotein B-containing lipoproteins. *Prog Retin Eye Res*. 2009;28(6):393–422.
77. DeBose-Boyd RA. Feedback regulation of cholesterol synthesis: sterol-accelerated ubiquitination and degradation of HMG CoA reductase. *Cell Res*. 2008; 18(6):609–621.
78. Pfrieger FW. Cholesterol homeostasis and function in neurons of the central nervous system. *Cell Mol Life Sci*. 2003;60(6):1158–1171.
79. Shaw G, Weber K. The intermediate filament complement of the retina: a comparison between different mammalian species. *Eur J Cell Biol*. 1984;33(1):95–104.
80. Dreher Z, Robinson SR, Distler C. Muller cells in vascular and avascular retinae: a survey of seven mammals. *J Comp Neurol*. 1992;323(1):59–80.
81. Madigan MC, Penfold PL, Provis JM, Balind TK, Billson FA. Intermediate filament expression in human retinal macroglia. Histopathologic changes associated with age-related macular degeneration. *Retina*. 1994;14(1):65–74.
82. Heckenlively JR, et al. Mouse model of subretinal neovascularization with choroidal anastomosis. *Retina*. 2003;23(4):518–522.
83. Okamoto N, et al. Transgenic mice with increased expression of vascular endothelial growth factor in the retina: a new model of intraretinal and subretinal neovascularization. *Am J Pathol*. 1997;151(1):281–291.
84. Chen Y, Hu Y, Moiseyev G, Zhou KK, Chen D, Ma JX. Photoreceptor degeneration and retinal inflammation induced by very low-density lipoprotein receptor deficiency. *Microvasc Res*. 2009;78(1):119–127.
85. Chen Y, Hu Y, Lu K, Flannery JG, Ma JX. Very low density lipoprotein receptor, a negative regulator of the wnt signaling pathway and choroidal neovascularization. *J Biol Chem*. 2007;282(47):34420–34428.
86. Zhou X, Wong LL, Karakoti AS, Seal S, McGinnis JF. Nanoceria inhibit the development and promote the regression of pathologic retinal neovascularization in the Vldlr knockout mouse. *PLoS One*. 2011;6(2):e16733.
87. Li C, et al. Biochemical alterations in the retinas of very low-density lipoprotein receptor knockout mice: an animal model of retinal angiomatous proliferation. *Arch Ophthalmol*. 2007;125(6):795–803.
88. Hua J, et al. Resveratrol inhibits pathologic retinal neovascularization in Vldlr(–/–) mice. *Invest Ophthalmol Vis Sci*. 2011;52(5):2809–2816.
89. Sirvent A, et al. The farnesoid X receptor induces very low density lipoprotein receptor gene expression. *FEBS Lett*. 2004;566(1–3):173–177.
90. Hu W, et al. Expression of VLDLR in the retina and evolution of subretinal neovascularization in the knockout mouse model's retinal angiomatous proliferation. *Invest Ophthalmol Vis Sci*. 2008;49(1):407–415.
91. Hong C, et al. The E3 ubiquitin ligase IDOL induces the degradation of the low density lipoprotein receptor family members VLDLR and ApoER2. *J Biol Chem*. 2010;285(26):19720–19726.
92. Janowski BA, et al. Structural requirements of ligands for the oxysterol liver X receptors LXRalpha and LXRbeta. *Proc Natl Acad Sci U S A*. 1999;96(1):266–271.
93. Song C, Liao S. Cholestenoic acid is a naturally occurring ligand for liver X receptor alpha. *Endocrinology*. 2000;141(11):4180–4184.
94. Janowski BA, Willy PJ, Devi TR, Falck JR, Mangelsdorf DJ. An oxysterol signalling pathway mediated by the nuclear receptor LXR alpha. *Nature*. 1996; 383(6602):728–731.
95. Spaide RF, Curcio CA. Anatomical correlates to the bands seen in the outer retina by optical coherence tomography: literature review and model. *Retina*. 2011;31(8):1609–1619.